


Linear electro-optic effect in trigonal LiNbO₃: A first-principles study

Inhwan Kim  and Alexander A. Demkov ^{*}

Department of Physics, The University of Texas, Austin, Texas 78712, USA

 (Received 15 November 2023; revised 22 January 2024; accepted 5 February 2024; published 28 February 2024)

Lithium niobate LiNbO₃ (LN) has emerged as a promising electro-optic (EO) material with applications in silicon photonics. It demonstrates a large linear EO response, often referred to as the Pockels effect. We report on a first-principles investigation of the origins of the Pockels response in *R3c* LN. We examine three contributions to the Pockels tensor, its electronic, ionic (Raman), and piezoelectric components, and demonstrate that the large value of Raman susceptibility can be traced to specific *A*₁ modes that affect the Nb-O bonding. To examine the origin of the piezoelectric Pockels response, we compute the elasto-optic and piezoelectric tensors. Importantly, the largest component of the Pockels tensor *r*₃₃ is dominated by the ionic response, which explains the insensitivity of the EO effect in LN to frequency.

DOI: [10.1103/PhysRevMaterials.8.025202](https://doi.org/10.1103/PhysRevMaterials.8.025202)

I. INTRODUCTION

The integration of optical components with traditional silicon technology—silicon photonics—has been growing rapidly, offering lower power consumption, faster speed, and larger bandwidth [1,2]. Si is transparent <1.1 eV, and waveguides fabricated in Si demonstrate optical loss of just 0.1 dB/m, making it an ideal material for fabricating integrated photonic devices with applications in optical communications, optical neuromorphic, and optical quantum computing. The ability to utilize existing fabrication infrastructure makes silicon photonics even more attractive. One of the key active photonic devices is an optical modulator, a device that controls either the amplitude or phase of light. Among the promising emerging modulators in integrated silicon photonics are the phase-shift modulators based on the linear electro-optic (EO) effect [2–6]. The linear EO or Pockels effect describes the linear change in the refractive index of the crystal under an external electric field [7]. It enables the design and fabrication of low-power, fast-field-effect devices. However, bulk silicon is centrosymmetric and therefore does not demonstrate the linear EO effect [8]. Strained Si has a weak linear EO response [4] and a quadratic or Kerr effect that is too small for practical applications. Thus, EO materials that can be integrated with Si and are compatible with stringent contamination requirements of Si fabrication facilities have attracted significant interest [9]. One such promising material, ferroelectric BaTiO₃ (BTO), has been recently studied both theoretically and experimentally due to its very high Pockels tensor component *r*₄₂ [8,10–13]. Thin-film BTO has also been successfully integrated into silicon photonics as a phase-shift modulator [1,13–17]. However, the most used EO material currently is another transition metal oxide ferroelectric, lithium niobate LiNbO₃ (LN) [18]. Trigonal LN has a large linear EO response and second-order nonlinear susceptibility, and it has

been adopted in telecommunications, optical modulators, and optical frequency converters [18–20]. Thin-film LN (TFLN) can be integrated onto the Si platform via wafer bonding [20]. The LN-based modulators demonstrate a low *VπL* (a common figure of merit defined as the voltage needed to achieve a phase shift of π for the given length of the device) of 2.2 V·cm, low loss (0.1 dB/cm), and high operating frequency (>100 GHz) [1].

Trigonal *R3c* LN is an order-disorder ferroelectric with a spontaneous polarization of 70 $\mu\text{C}/\text{cm}^2$ below its Curie temperature of 1400 K [18]. It has the *R3c* space group with *3m* point group symmetry. The experimental lattice constants are $a = b = c = 5.433^\circ$ with angles $\alpha = \beta = \gamma = 55.918^\circ$ [21]. Both the primitive and conventional unit cells are shown in Fig. 1. The fractional atomic coordinates for the trigonal LN primitive cell are given in Table I. The theoretically optimized lattice constant of 5.477 Å and angle of 55.867° are reasonably close to the experimental values. In bulk, the displacements of Li ions play the main role in establishing the ferroelectric polarization. Below the Curie temperature, the Li ions move upward (or downward as a mirror image) with respect to the triangular oxygen plane, resulting in the spontaneous electric polarization along the *c* axis.

First-principles calculations have been successfully used to explain the mechanism of the linear EO (Pockels) response in several oxides [9–11,22–25]. Here, we report on a first-principles analysis of the linear EO response in *R3c* LN. We consider both clamped and unclamped Pockels tensors and explore the contribution of the piezoelectric effect. While the total magnitude of the unclamped EO tensor is well known [22], the specific contributions of the ionic and piezoelectric effects to the Pockels tensor remain unexamined. In a ferroelectric such as LN, the Pockels tensor has three distinct components—electronic, ionic, and piezoelectric, as all ferroelectric materials are piezoelectric below the Curie temperature [22]. For example, in both low-temperature rhombohedral and room-temperature tetragonal BTO, the Pockels effect is driven in approximately equal measure by

^{*}demkov@physics.utexas.edu

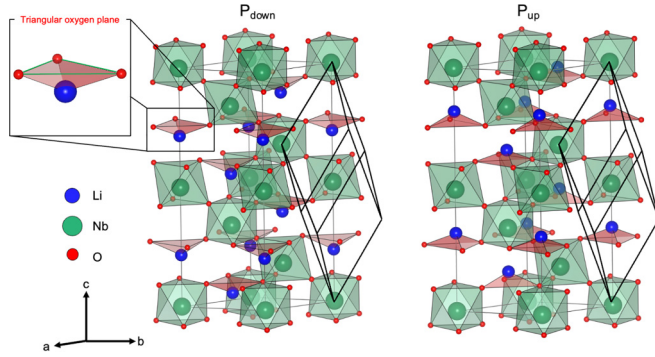


FIG. 1. Crystal structure of the conventional and primitive trigonal $R3c$ LiNbO_3 . The ferroelectricity is induced by displacements of Li ions along the c axis with respect to the plane defined by the three neighboring oxygen ions.

the ionic and piezo or lattice responses, with the electronic contribution playing a relatively minor role. The ionic Pockels response in BTO is driven primarily by the low frequencies of the relevant optical phonon modes [10,26]. In contrast to BTO, as we shall demonstrate later, LN lacks a significant Raman response from the lowest frequency optical modes. While the optical phonons are responsible for the high-frequency behavior, the lattice or piezoelectric response controls the low-temperature behavior when the optical modes are frozen out. Little is known about the details of the Pockels effect in LN at the microscopic level, which is the focus of our study. The rest of the paper is organized as follows. Firstly, we briefly introduce the theoretical framework for computing the Pockels response. This is followed by a comprehensive analysis of the microscopic origins of the ionic and piezoelectric contributions to the EO response in $R3c$ LN.

II. BACKGROUND AND METHODS

The Pockels effect refers to the crystal refractive index change by an applied electric field that is linear in the field [7]. It is expressed as a change of the optical indicatrix as follows [27]:

$$\Delta\left(\frac{1}{n_{ij}^2}\right) = \Delta(\varepsilon^{-1})_{ij} = \sum_{\gamma} r_{ij\gamma} E_{\gamma}, \quad (1)$$

TABLE I. Theoretical fractional atomic coordinates for $R3c$ LiNbO_3 .

Element	x	y	z
Nb ₁	0	0	0
Nb ₂	0.5	0.5	0.5
Li ₁	0.217	0.217	0.217
Li ₂	0.717	0.717	0.717
O ₁	0.894	0.63	0.283
O ₂	0.283	0.894	0.63
O ₃	0.63	0.283	0.894
O ₄	0.131	0.394	0.783
O ₅	0.783	0.131	0.394
O ₆	0.394	0.783	0.131

where n_{ij} is refractive index, $(\varepsilon^{-1})_{ij}$ is the inverse of the electronic dielectric tensor, $r_{ij\gamma}$ the linear EO tensor (or Pockels tensor) and i, j , and γ stand for Cartesian coordinates. The first two indices refer to the indicatrix and the third to the electric field. The Pockels tensor can also be written as the first-order change in the electronic dielectric tensor induced by an applied electric field E_{γ} [28]:

$$d\varepsilon_{ij} = - \sum_k r_{ij\gamma} \varepsilon_{ii} \varepsilon_{jj} dE_{\gamma}(\omega). \quad (2)$$

A detailed description of the Pockels response in the framework of density functional theory (DFT) can be found in Refs. [10,22,29]. Because all ferroelectric materials are also piezoelectric, the Pockels tensor in LN can be split up into three contributions: electronic, ionic or Raman, and lattice or piezoelectric. The electronic response comes from the interaction of the electric field with valence electrons, assuming the ions are fixed at their equilibrium positions. It is related to the second harmonic generation effect and is proportional to $\chi_{ij}^{(2)}$ [9]. Interestingly, LN has a large nonlinear susceptibility response which contributes $\sim 20\%$ of the Pockels response ($r_{33}^{\text{unclamped}}$), which is unusually large compared with other EO materials [30].

The ionic term captures the change in the dielectric susceptibility tensor induced by shifts in the atomic positions in response to the applied electric field. It can be expressed as [22]

$$r_{ij\gamma}^{\text{ion}} = - \frac{4\pi}{n_i^2 n_j^2} \sum_m \frac{1}{\omega_m^2} \left[\sum_{\kappa\alpha} \frac{\partial \chi_{ij}^{(1)}}{\partial \tau_{\kappa\alpha}} u_m(\kappa\alpha) \right] \times \left[\sum_{\kappa'\beta} Z_{\kappa'\gamma\beta}^* u_m(\kappa'\beta) \right], \quad (3)$$

where n_i is the principal refractive index, $\chi_{ij}^{(1)}$ is the linear electronic dielectric susceptibility, and $\tau_{\kappa\alpha}$ refers to a displacement of atom κ in the α direction. Here, $Z_{\kappa'\gamma\beta}^*$ is the Born effective charge, where γ is the component of the field, and $u_m(\kappa'\beta)$ is the mass-normalized eigendisplacement component of mode m , describing atom κ' shifting in the β direction. Also, ω_m is the frequency of mode m , and Ω_o is the unit cell volume. Equation (3) can be simplified as

$$r_{ij\gamma}^{\text{ion}} = - \frac{4\pi}{\sqrt{\Omega_o} n_i^2 n_j^2} \sum_m \frac{\alpha_{ij}^m p_{m,\gamma}}{\omega_m^2}. \quad (4)$$

The expression in the first bracket of Eq. (3) is the Raman susceptibility α_{ij}^m divided by $\sqrt{\Omega_o}$. It describes the modulation of the linear dielectric susceptibility $\chi^{(1)}$ by lattice vibrations [31]. In the second bracket is the mode polarity $p_{m,\gamma}$, the Born effective charge multiplied by a phonon eigendisplacement, that describes the dipole moment associated with each mode.

The piezoelectric contribution is the third and final part of the Pockels tensor, describing the effect of strain caused by the converse piezoelectric effect on susceptibility. If the frequency of the applied electric field is sufficiently high, the EO response will be *clamped*, referring to the lattice vectors staying fixed as the driving frequency is too high for the lattice to follow. We assume the applied field frequency is

low enough to trigger the converse piezoelectric effect and compute the so-called unclamped response. It can be written in terms of the clamped Pockels tensor $r_{ij\gamma}^\eta$, the piezoelectric strain coefficients $d_{\mu\nu\gamma}$, and elasto-optic coefficients $p_{ij\mu\nu}$:

$$r_{ij\gamma}^\sigma = r_{ij\gamma}^\eta + \sum_{\mu,\nu=1}^3 p_{ij\mu\nu} d_{\mu\nu\gamma}. \quad (5)$$

The piezoelectric strain tensor can be calculated directly using first-principles software packages such as ABINIT or VASP. To determine the elasto-optic tensor, we use the finite difference method to compute the derivatives of the inverse dielectric tensor with respect to strain [32,33]. We can rewrite the second term of Eq. (5) in terms of the inverse dielectric tensor and convert the derivative into a finite-difference form:

$$\Delta(\varepsilon^{-1})_{ij}^{\text{piezo}} = \sum_{\mu,\nu=1}^3 p_{ij\mu\nu} \eta_{\mu\nu}. \quad (6)$$

$$p_{ij\mu\nu} \approx \frac{\Delta(\varepsilon^{-1})_{ij}(\eta^+) - \Delta(\varepsilon^{-1})_{ij}(\eta^-)}{2\eta_{\mu\nu}} + O(\eta^3). \quad (7)$$

Here, $\eta_{\mu\nu}$ is the (μ,ν) element of the strain tensor describing the lattice distortion due to the electric field. The computational procedure is as follows. First, the high-frequency dielectric tensor is calculated in the equilibrium configuration. Then the lattice vectors are strained, and the internal coordinates relax in this new unit cell. We compute the dielectric tensor for unit cells under different strain values, then evaluate Eq. (7) using a centered, finite-difference derivative with respect to the parametrized strain. The second term in Eq. (7) represents higher-order terms that are neglected.

All calculations are performed using DFT with the plane-wave-based ABINIT software package [34–38]. The local density approximation (LDA) is employed for the exchange-correlation term [39]. We use norm-conserving pseudopotentials that include valence electron shells of $1s_2 2s_1$ for the lithium atoms, $4s_2 4p_6 4d_4 5s_1$ for the niobium atoms, and $2s_2 2p_4$ for the oxygen atoms [40]. Both the lattice parameters of the cell and the internal atomic coordinates are fully relaxed before the Pockels tensor calculation. The crystal structures are optimized with a force convergence of 1×10^{-4} eV/atom, while the energy criterion is 1×10^{-7} eV. A plane-wave cutoff energy of 1000 eV is used with a $12 \times 12 \times 12$ Monkhorst-Pack grid for the Brillouin zone integration [41]. We adapt the $2n + 1$ theorem using density functional perturbation theory (DFPT) to calculate the clamped Pockels tensor [10,22]. To gain a better understanding of our Raman susceptibility results, we repeat the calculations with the VASP and PHONOPY software packages [42–46]. The projector augmented-wave potentials with the LDA exchange-correlation term are used with the same configuration of valence electrons as ABINIT [47]. Also, the same force and energy criteria are considered with a cutoff energy of 600 eV and a $12 \times 12 \times 12$ Monkhorst-Pack grid. To calculate first-order electronic susceptibility, we use cutoff energy of 1000 eV and a $10 \times 10 \times 10$ k -point grid to ensure convergence of 1×10^{-5} . This is necessary when using finite difference to calculate derivatives of $\chi^{(1)}$. We use a $3 \times 3 \times 3$ supercell to calculate the interatomic force constants for each finite-difference set. The full phonon dispersion is computed using PHONOPY [48].

TABLE II. Calculated nonlinear optical coefficient d_{ij} for $R3c$ LiNbO_3 .

Element (pm/V)	This paper	Experiment [18]
d_{22}	1.5	3
d_{31}	8.6	5.9
d_{33}	29	30

III. RESULTS AND DISCUSSION

Before we start the discussion of the Pockels tensor, let us point out some of its general properties. The Pockels effect is described by a third rank tensor and has three indices. The first two indices describe the optical indicatrix of the material, and the last one indicates the direction of the external electric field. Because the Pockels tensor is symmetric in the first two indices, one can merge them into a single index. Thus, in this paper, we use the Voigt notation for the first two indices of the Pockels tensor [7]. We investigate both the clamped and unclamped Pockels effects that can be measured separately by changing the frequency of the external electric field. We start our discussion with the clamped Pockels tensor, which is the sum of electronic and ionic Pockels tensor contributions. Usually, the electronic part of the Pockels tensor is expressed as the nonlinear optical coefficient tensor d_{ij} after applying the Voigt notation for the last two indices, which is $\chi_{ij}^{(2)}$ divided by two [22]. Note that, due to symmetry, there are only three nonzero elements $d_{22} = -d_{21} = -d_{16}$, $d_{31} = d_{32} = d_{24} = d_{15}$, and d_{33} under the $R3c$ space group. The linear EO tensor in the $R3c$ space group has four independent elements: r_{113} , r_{333} , r_{222} , and r_{131} . However, the nonlinear optical coefficient tensor d_{ijk} has only three independent elements: d_{22} , d_{31} , and d_{33} , because $d_{ijk} = \frac{1}{2} \chi_{ijk}^{(2)}$ in $R3c$ symmetry $d_{31} = d_{32} = d_{24} = d_{15}$. Because the electronic EO tensor is defined as $r_{ijk}^{\text{elec}} = \frac{8\pi}{n_i n_j} \chi_{ijk}^{(2)}$, r_{13}^{elec} and r_{51}^{elec} are no longer equal, and there are four independent elements for the EO tensor. We list the nonlinear optical coefficient tensor components in Table II along with the experimental values from Ref. [18]. As one can see from the table, the agreement is fair, with d_{33} being the closest to experiment (29 pm/V vs the experimental value of 30 pm/V).

According to Eq. (3), the ionic Pockels tensor is a product of the inverse square of the optical phonon Γ -point frequency ω_m^2 , Raman susceptibility, and the mode polarity summed over all optical modes. Therefore, the critical step of calculating the ionic response comes from a careful analysis of the low-frequency phonon modes. In Fig. 2, we show the calculated phonon dispersion of the ground state $R3c$ LN. We obtain the Γ -point optical phonon frequencies from the DFPT calculation (results are listed in Table III; all the E modes are doubly degenerate). We include the Lydanne-Sachs-Teller corrections [52] for the phonon dispersion, while the short-range (excluding long-range Coulomb effects) frequencies are used in the ionic Pockels tensor calculation. We compare the ABINIT (DFPT) results with those obtained using VASP calculated using a finite-difference method with a value of 0.01\AA for the displacement. The symmetry and the corresponding optical phonon frequencies at the Γ point are

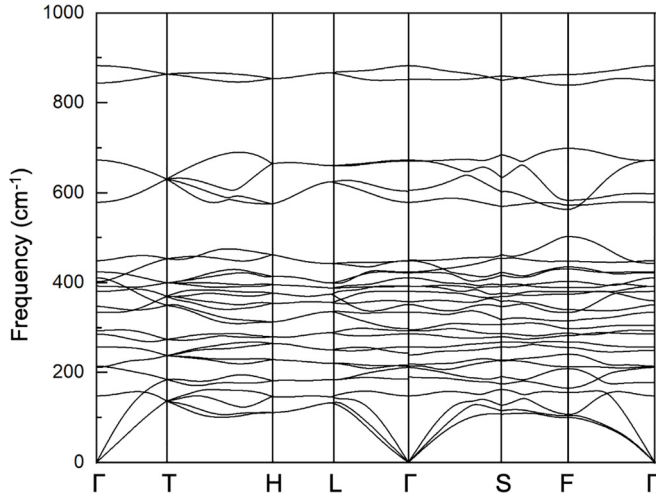


FIG. 2. Phonon dispersion of $R3c$ LiNbO_3 . The long-range Coulomb interaction correction that splits longitudinal and transverse optical modes is considered at the Γ point.

reported in Table III. The optical modes at the high-symmetry Γ point are described by the symmetry representation $\Gamma = 4A_1 + 9E + 5A_2$, with the E modes exhibiting double degeneracy (27 optical modes in total). While both A_1 and E modes display Raman and infrared (IR) activity, the remaining five A_2 modes are expected to be Raman/IR inactive and can be detected by inelastic neutron scattering [49,53]. Except for the order of the first A_2 mode and the second E mode, both methods give the same result. Surprisingly, once combined with the Raman susceptibility and the mode polarity, it is not the lowest frequency mode (mode 4) but mode 9 that shows the highest contribution to the ionic Pockels tensor. Note that, even though there is the ω_m^2 term in the denominator, the

TABLE III. Mode symmetry and frequencies of $R3c$ LiNbO_3 using ABINIT and VASP. The numbers in parentheses indicate the mode number.

Mode	ABINIT (cm ⁻¹)	VASP (cm ⁻¹)	Experiment [49–51] (cm ⁻¹)	
A_1	239 (9)	239 (9)	256 [50]	
	285 (12)	286 (12)	275 [50]	
	359 (16)	357 (16)	332 [50]	
	609 (27)	606 (27)	637 [50]	
	152 (4, 5)	148 (4, 5)	155 [51]	
E	215 (7, 8)	212 (6, 7)	238 [51]	
	262 (10, 11)	258 (10, 11)	265 [51]	
	335 (14, 15)	334 (14, 15)	325 [51]	
	378 (17, 18)	380 (17, 18)	371 [51]	
	390 (19, 20)	392 (19, 20)		
	434 (22, 23)	424 (22, 23)	431 [51]	
	582 (25, 26)	579 (25, 26)	582 [51]	
	672 (28, 29)	673 (28, 29)	668 [51]	
	A_2	207 (6)	214 (8)	224 [49]
		297 (13)	293 (13)	314 [49]
415 (21)		411 (21)		
456 (24)		449 (24)	455 [49]	
892 (30)		883 (30)		

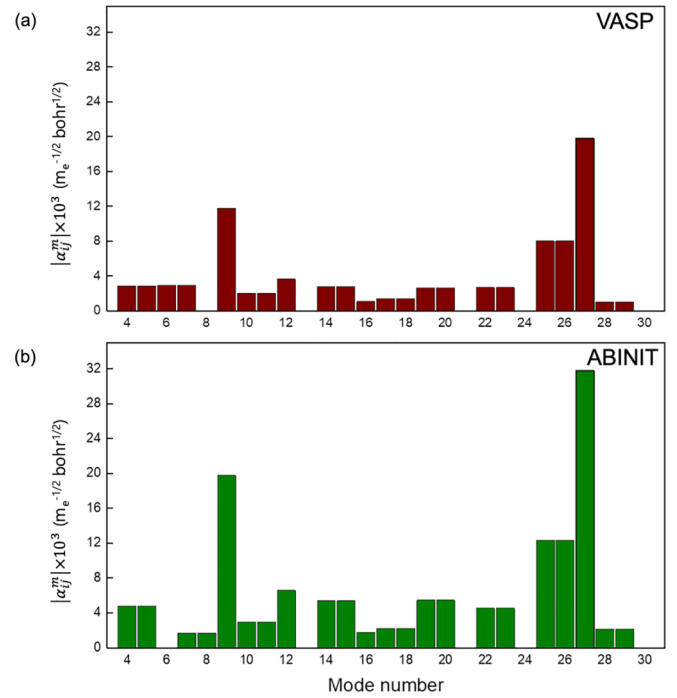


FIG. 3. The maximum component of the Raman susceptibility for each optical mode from the (a) finite difference method (VASP) and the (b) density functional perturbation theory (ABINIT). Note that modes 9 and 27 have the largest Raman susceptibility values among other optical modes that induce a large ionic Pockels response. All the A_2 modes are captured in both VASP and ABINIT.

lowest frequency modes, 4 and 5, only contribute 7.9 pm/V out of 36.9 pm/V to the $r_{42}^{\text{unclamped}}$ Pockels tensor component and 3.4 pm/V out of 13.5 pm/V to the $r_{22}^{\text{unclamped}}$ Pockels tensor component. This suggests that, in addition to the value of the optical phonon frequency, a careful analysis of the Raman susceptibility tensor, capturing the electron-phonon coupling is needed to understand the origin of the linear EO response.

To obtain $\frac{\partial \chi_{ij}}{\partial r_{\kappa\alpha}}$, we compute the optical dielectric tensor (and thus the first-order electronic susceptibility). Again, we compare our results between ABINIT that uses DFPT and VASP using the finite-difference method. In the latter, we slightly displace atoms along the eigendisplacement direction with the magnitude of 0.01 Å and subsequently compute the variation in electronic susceptibility using a second-order derivative formula (this is the reason for tighter convergence criterion for susceptibility). Figure 3 shows the largest component of the Raman susceptibility tensor for each optical mode. Mode 9 shows the largest ionic Pockels response, 14 pm/V out of 27 pm/V for the r_{33}^{clamped} component. Note that, while mode 27 has a rather large Raman susceptibility, the relatively high optical phonon frequency of 605 cm⁻¹ suppresses the ionic Pockels response, and the mode contributes only 5 pm/V to r_{33} . In the case of the silent modes, however, all the A_2 modes are expected to have zero Raman susceptibility values. This implies that the change in the electronic susceptibility χ_{ij} due to the atomic displacements along the A_2 eigendisplacement mode is expected to be zero. This analysis agrees with the selection rules for a crystal with C_{3v} point group symmetry

[51]. Indeed, all five A_2 modes show zero Raman susceptibility in both the finite-difference method (VASP) and DFPT (ABINIT).

The fact that mode 9 is special has already been noticed by Veithen and Ghosez [54]. They have shown that the lowest imaginary A_{2u} mode that drives the ferroelectric distortion in the paraelectric phase exhibits a substantial overlap with A_1 mode 9 of the ferroelectric phase. Indeed, we find that there is 0.92 overlap between these two modes. In other words, when the crystal goes to the dynamically stable ferroelectric phase, the very same mode drives the large Pockels response. Another interesting observation is that the lowest-frequency E modes (4 and 5) have a relatively unimpressive Raman susceptibility and, as a result, do not contribute much to the EO response. This is different from what one finds in titanates, where the lowest-frequency optical mode is the main driver. The reason turns out to be crystallographic or quantum mechanical, depending on how deep one chooses to look. Modes 4 and 5 are what one may call the rigid unit modes (RUMs) [55]. In such modes, the structural polyhedra do not change their shape and move as a solid unit. This lack of the relative movement of Nb and oxygen atoms results in a very minor change of the near-edge electronic spectrum. That in turn causes only a minor change in the electronic susceptibility $\chi^{(1)}$, which is what the Raman susceptibility measures. In BTO, the low-frequency mode is not an RUM but the ferroelectric Ti-O displacement mode due to a rather special nature of the Ti-O bonding [56].

Previous studies have demonstrated that LN exhibits an order-disorder type ferroelectric transition and that the paraelectric phase is a result of the equal occupation of polarization up and down states above the Curie temperature (1400 K for LN) [54,57,58]. Even though LN is considered an order-disorder ferroelectric, all previous theoretical studies used the static centrosymmetric structure for the paraelectric phase [54,58]. In an attempt to account for the dynamic nature of paraelectric LN, we consider three possible configurations that can be averaged to produce a paraelectric structure: (1) centrosymmetric configuration (does not need averaging), (2) antiferroelectric configuration, and (3) a combination of two ferroelectric phases with opposite polarization direction. It is assumed that, in configurations (2) and (3), the system oscillates rapidly between two oppositely polarized states. All configurations are fully optimized before we compute the derivatives of susceptibility. First, we discuss the centrosymmetric phase. As shown in the inset of Fig. 4(a), the centrosymmetric configuration has no ferroelectric displacement, and susceptibility shows a complete lack of response to Nb displacements. When we consider the antiferroelectric configuration, the Li atoms are displaced along the c axis in opposite directions, while the Nb atoms remain at the center of surrounding oxygen octahedra. In Fig. 4(b), we again see that the displacement of the Nb atoms does not contribute to a change in the dielectric susceptibility, like what we observe in the paraelectric configuration. Interestingly, the lowest imaginary mode in the antiferroelectric state exhibits even larger overlap of 0.97 with mode 9 of the ferroelectric state. Lastly, we consider the ferroelectric configuration. Here, both Li and Nb atoms are displaced in the same direction. The derivative of dielectric susceptibility in Fig. 4(c) shows a significant

response when a Nb atom is displaced, particularly in the z direction. Nevertheless, even though there is a substantial response contributing to the Raman susceptibility, the existence of an equal number of polarization up and down states leads to a zero Pockels response on average. The conclusion is that, when the mode driving ferroelectricity condenses producing a ferroelectric state, the susceptibility becomes very sensitive to Nb displacement. This large response is the dominant contributor to Raman susceptibility.

From the electronic structure point of view, the value of the Raman susceptibility is largely controlled by the sensitivity of the electronic spectrum to the mode atomic displacement; the leading term is related to the smallest energy difference in the spectrum, which is the band gap [10]. To elucidate why modes 9 and 27 have such a large Raman susceptibility and A_2 modes have nearly zero Raman susceptibility at the microscopic level, we compare the electronic band gap change in response to displacing the atoms along the eigenvectors of the corresponding modes. In Fig. 5, we plot the band gap change as a function of the displacement amplitude. This is achieved by scaling the normalized mode eigenvector from 0 to 0.03Å. The plot shows that the active mode closes the band gap notably, while the inactive mode 6 barely changes the band gap. Mode 27, which has the largest change, shows the biggest band gap change, 0.15 eV for the maximum atomic displacement. Meanwhile, mode 6 (A_2), which has zero Raman susceptibility, hardly causes any change in the band gap. In this calculation, we can clearly observe that modes 9 and 27 have specific eigenmode patterns that change the electronic structure significantly, inducing the large change in the dielectric susceptibility tensor.

To further understand this spectral change, we plot the phonon eigenmode pattern in the primitive cell in Fig. 6. The Raman active modes 9 and 27 exhibit out-of-phase displacement patterns between the Li and O atoms and Nb and O atoms. As previously studied by Veithen and Ghosez [54], the Nb $4d$ and O $2p$ atomic orbitals strongly interact to form the valence and conduction bands near the band edge, while the Li atoms completely lose their $2s$ electrons. As a result, the valence band near the edge is primarily occupied by O $2p$ orbitals, while the lowest conduction band is predominantly composed of Nb $4d$ orbitals [54]. Therefore, the out-of-phase displacement pattern of modes 9 and 27 are expected to bring substantial modification of the orbital overlaps between the niobium d and oxygen p states. This altered overlap between the Nb and O atoms, in turn, has a significant impact on the hopping integral, leading to considerable shifts in the band gap, resulting in a large Raman susceptibility [10].

Let us now discuss the mode polarity $p_{m,\gamma}$, as it is the last part of the ionic Pockels tensor. Figure 7 shows the value of polarity for each optical mode. The x and y components have the same values for all optical modes due to symmetry. Also note that the Born effective charge in Eq. (3) is the same for all phonon modes, and the only difference is the eigenmode itself. As can be seen in the figure, a large mode polarity value does not necessarily guarantee a large Pockels response. Note that modes 17, 19, and 20 have the largest values but have small Raman susceptibility, and due to a higher phonon frequency and relatively small Raman susceptibility, these modes do not contribute to the Pockels response. Previous theoretical

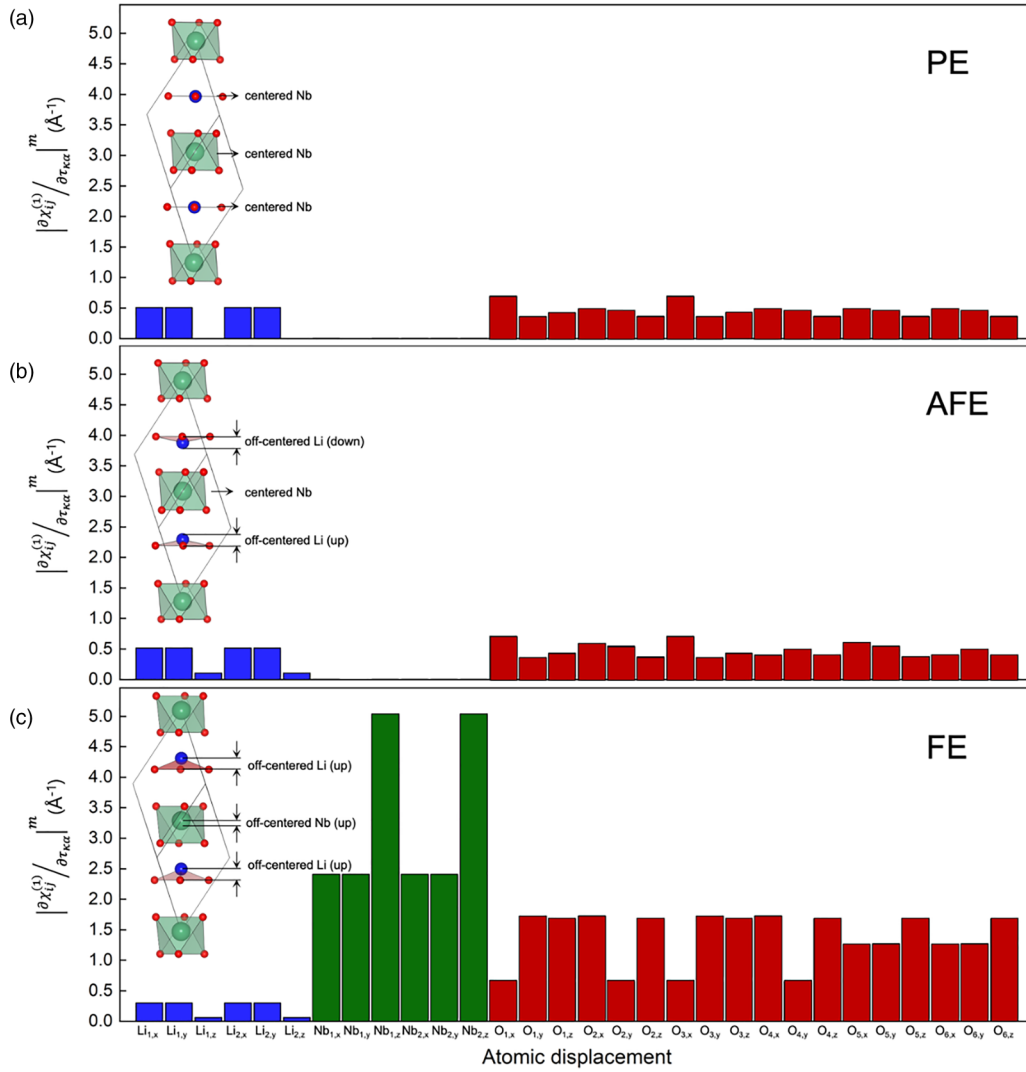


FIG. 4. The variation of the dielectric susceptibility tensor with respect to each atomic displacement along the x , y , and z directions, represented in Eq. (3), is computed using the finite difference method for the (a) paraelectric, (b) antiferroelectric, and (c) ferroelectric phases. Before applying the atomic displacement, each configuration is fully optimized. Note that only the ferroelectric phase exhibits a response to the Nb atoms due to the off-centered ferroelectric distortion, while the paraelectric and antiferroelectric phases exhibit no response with Nb atom displacements, and all the Nb atoms are located in the middle of the oxygen octahedra.

studies have shown that even larger values of the mode polarity can still result in a small EO response [9,10].

Because the optical phonon frequency appears as a square factor in the denominator of the ionic Pockels tensor calculation, only the lower-frequency modes are more likely to contribute significantly to the Pockels response. However, even though mode 9 has a larger frequency of 238cm^{-1} compared with other low-frequency modes, it has the largest contribution to the ionic Pockels tensor, especially to the r_{33}^{clamped} component. In Table IV, we list the electronic and clamped Pockels tensor components (a sum of the electronic and ionic parts), computed for $R3c$ LiNbO_3 . Note that the r_{33} component has both the strongest electronic and ionic response of any other component of the Pockels tensor.

Let us now discuss the piezo contribution to the Pockels response. According to Eq. (5), it is a sum over the products of

the piezoelectric strain tensor $d_{\gamma\mu\nu}$ and the fourth-rank elasto-optic tensor $p_{ij\mu\nu}$. Like the Pockels tensor, the piezoelectric strain tensor is also symmetric in the first two indices. The elasto-optic tensor is symmetric in the first two and last two indices, and it can be collapsed to only two indices $p_{ij\mu\nu} \rightarrow p_{i\mu}$. The results of our ABINIT calculation can be found in Tables IV and V. The piezoelectric strain tensor $d_{\gamma\mu\nu}$ is calculated by multiplying the compliance tensor $s_{\gamma\mu mn}$ and the piezoelectric stress tensor e_{mnv} using the relationship between the strain and stress [7]. The only nonzero elements for the piezoelectric strain tensor are d_{22} , d_{13} , d_{33} , and d_{42} . Note that the large d_{42} component will significantly contribute to $r_{42}^{\text{unclamped}}$ when combined with the elasto-optic tensor. Both the piezoelectric stress tensor and the compliance tensor can be directly calculated using DFPT implemented in ABINIT [22]. As one can see in Table V, the calculated values show good agreement with experiment [21].

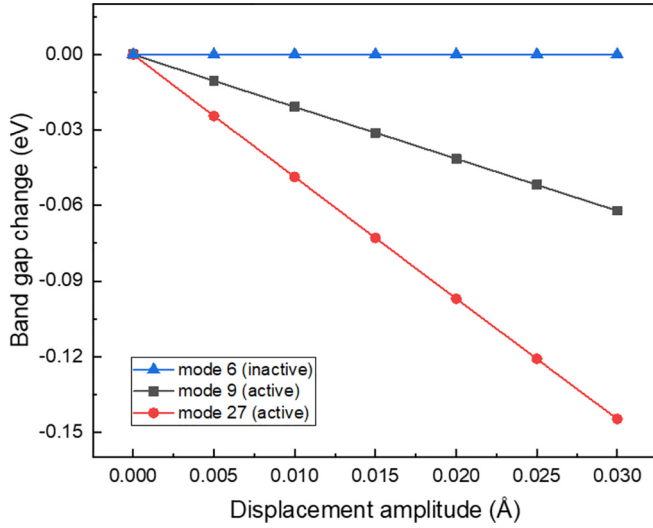


FIG. 5. The band gap change with respect to the magnitude of displacement for two Raman active modes (mode 9 and 27) and one inactive (mode 6).

The last element needed for the piezo part and for the unclamped Pockels tensor is the elasto-optic tensor p_{ijkl} . As discussed above, we calculate the elasto-optic tensor using the finite-difference method (Eq. (7)). As one can see in Table VI, some components are very close to experimental values, and the overall agreement with experiment is fair. Adding together the electronic, ionic, and piezo parts of the Pockels tensor, we obtain the total unclamped Pockels tensor components listed in Table VI.

When we compare with the experimental unclamped Pockels tensor, we find good agreement. Weis and Gaylord [21] report values of $r_{22}^{\text{unclamped}} = 9.89$ pm/V, $r_{13}^{\text{unclamped}} = 10$ pm/V,

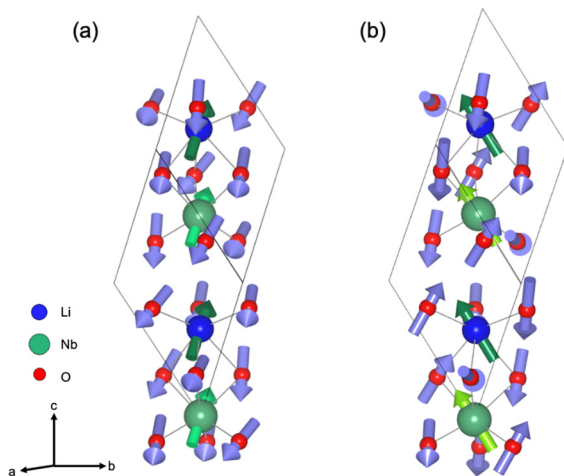


FIG. 6. The eigenmode pattern of $R3c$ LiNbO₃ for the (a) Raman active mode 9 and (b) Raman active mode 27 shown in the primitive cell. Both modes exhibit an out-of-phase displacement pattern between the Nb and O atoms. In both modes, Li and Nb atoms move in the same direction. While mode 9 is a relative displacement of the metal and oxygen sublattices, oxygen movement in mode 27 is complex.

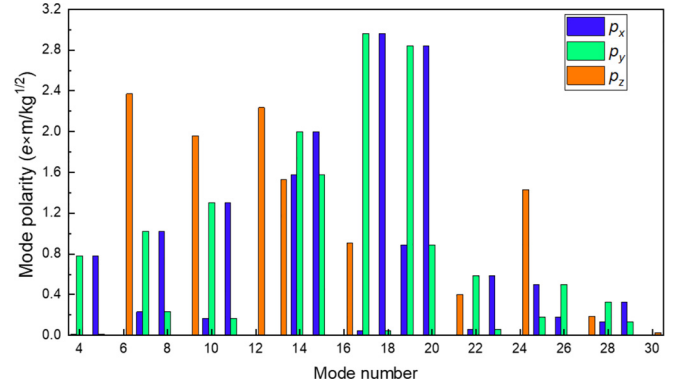


FIG. 7. Mode polarities of the $R3c$ LiNbO₃ at the Γ point for each optical mode.

$r_{33}^{\text{unclamped}} = 32.2$ pm/V, and $r_{42}^{\text{unclamped}} = 32.6$ pm/V [59,60]. Interestingly, the specific contributions to the unclamped Pockels tensor for each component in $R3c$ LNO vary. For instance, the $r_{13}^{\text{unclamped}}$ and $r_{33}^{\text{unclamped}}$ elements originate primarily from the ionic response. This suggests that this component could be used at relatively high frequencies. On the other hand, almost half of the $r_{42}^{\text{unclamped}}$ component is coming from the piezoelectric Pockels response, driven by the large value of the piezoelectric strain and the elasto-optic component. The remaining half comes from the ionic response (it exhibits the largest unclamped Pockels response). Thus, one would expect the performance of a device using this component to be somewhat diminished at high frequencies as, above the acoustic resonance, the piezoeffect will taper off. On the other hand, it may still be sizable at low frequency down to cryogenic temperatures.

IV. CONCLUSIONS

We report on the detailed theoretical analysis of the Pockels effect in $R3c$ LiNbO₃, finding good agreement with experiment, and providing insight into the origins of the EO response. Interestingly, the lowest-frequency optical modes do not contribute to the ionic Pockels response significantly, but the large Raman susceptibility of mode 9 is the main driver of the ionic Pockels response. This mode boasts a winning combination of a modest frequency and displacement pattern that triggers a large change in the electronic spectrum and, consequently, in the dielectric tensor. In the paraelectric phase, most Raman susceptibility values are suppressed because of either the minimal response of dielectric

TABLE IV. Electronic and clamped contribution to the Pockels tensor r_{ij} for $R3c$ LiNbO₃ in Voigt notation.

Electronic Pockels tensor (pm/V)			Clamped Pockels tensor (pm/V)		
0	-0.21	1.15	0	-5.53	10.5
0	0.21	1.15	0	5.53	10.5
0	0	4	0	0	27
0	1.19	0	0	17	0
1.19	0	0	17	0	0
-0.21	0	0	-5.53	0	

TABLE V. The piezoelectric strain tensors obtained through ABINIT and experiment [21].

Element	This paper (pC/N)	Experiment (pC/N)
d_{22}	22	21
d_{13}	-0.16	-0.1
d_{33}	7.8	6
d_{42}	67	68

susceptibility to the atomic displacements or being averaged out to zero in the order-disorder configuration. In addition, we compute the piezoelectric Pockels response after computing the elasto-optic and piezoelectric strain tensors in good agreement with experiment. We find the piezo part of the Pockels tensor fairly close to the experimental values and obtain $r_{22}^{\text{unclamped}} = 13.5$ pm/V, $r_{13}^{\text{unclamped}} = 12.4$ pm/V, $r_{33}^{\text{unclamped}} = 28.1$ pm/V, and $r_{42}^{\text{unclamped}} = 36.9$ pm/V for the unclamped Pockels tensor. Notably, $r_{13}^{\text{unclamped}}$ and $r_{33}^{\text{unclamped}}$ components are driven primarily by the ionic (or Raman) response, suggesting a weak frequency dependence as the piezo contribution that is lost above the acoustic resonance is initially minor. In contrast, the $r_{22}^{\text{unclamped}}$ and $r_{42}^{\text{unclamped}}$ components exhibit relatively large piezocontribution wherein >50% of the unclamped Pockels responses is driven by the large values of piezoelectric and elasto-optic tensors. This suggests that these tensor components may be suppressed at high frequency.

TABLE VI. Unique elements of the elasto-optic tensor (unitless) and the unclamped Pockels tensor components obtained through theory and experiment [21,59,60].

Elasto-optic element	This work	Experiment
p_{11}	0.0292	0.025 [21]
p_{12}	0.0594	0.079 [21]
p_{13}	0.175	0.133 [21]
p_{31}	0.147	0.179 [21]
p_{33}	0.136	0.071 [21]
p_{44}	0.177	0.15 [21]
p_{14}	-0.09	-0.075 [21]
p_{41}	-0.18	-0.151 [21]
$r_{22}^{\text{unclamped}}$ (pm/V)	13.5	6.8 [59], 9.89 [60]
$r_{13}^{\text{unclamped}}$ (pm/V)	12.4	10 [59]
$r_{33}^{\text{unclamped}}$ (pm/V)	28.1	32.2 [59]
$r_{42}^{\text{unclamped}}$ (pm/V)	36.9	32.6 [59]

ACKNOWLEDGMENTS

We thank Agham Posadas for the critical reading of the manuscript and Sohm Apte for many insightful discussions. This paper is supported by the Air Force Office of Scientific Research (AFOSR) under Award No FA9550-18-1-0053 and in part by a Multidisciplinary University Research Initiative (MURI) from the Air Force Office of Scientific Research (AFOSR MURI Award No. FA9550-22-1-0307).

- [1] A. Rahim, A. Hermans, B. Wohlfeil, D. Petousi, B. Kuyken, D. Van Thourhout, and R. Baets, Taking silicon photonics modulators to a higher performance level: State-of-the-art and a review of new technologies, *Adv. Photonics* **3**, 024003 (2021).
- [2] A. A. Demkov and A. B. Posadas, Si-integrated ferroelectrics for photonics and optical computing, *MRS Bull.* **47**, 485 (2022).
- [3] K. Vandoorne, P. Mechet, T. Van Vaerenbergh, M. Fiers, G. Morthier, D. Verstraeten, B. Schrauwen, J. Dambre, and P. Bienstman, Experimental demonstration of reservoir computing on a silicon photonics chip, *Nat. Commun.* **5**, 3541 (2014).
- [4] G. T. Reed, G. Mashanovich, F. Y. Gardes, and D. J. Thomson, Silicon optical modulators, *Nat. Photon.* **4**, 518 (2010).
- [5] M. J. R. Heck, H. W. Chen, A. W. Fang, B. R. Koch, D. Liang, H. Park, M. N. Sysak, and J. E. Bowers, Hybrid silicon photonics for optical interconnects, *IEEE J. Sel. Top. Quantum Electron.* **17**, 333 (2011).
- [6] M. Li and H. X. Tang, Strong Pockels materials, *Nat. Mater.* **18**, 9 (2019).
- [7] J. F. Nye, *Physical Properties of Crystals: Their Representation by Tensors and Matrices* (Oxford University Press, Oxford, 1985).
- [8] W. Guo, A. B. Posadas, and A. A. Demkov, Epitaxial integration of BaTiO₃ on Si for electro-optic applications, *J. Vac. Sci.* **39**, 030804 (2021).
- [9] A. K. Hamze, M. Reynaud, J. Geler-Kremer, and A. A. Demkov, Design rules for strong electro-optic materials, *npj Comput. Mater.* **6**, 130 (2020).
- [10] T. Paoletta and A. A. Demkov, Pockels effect in low-temperature rhombohedral BaTiO₃, *Phys. Rev. B* **103**, 014303 (2021).
- [11] K. D. Fredrickson, V. V. Vogler-Neuling, K. J. Kormondy, D. Caimi, F. Eltes, M. Sousa, J. Fompeyrine, S. Abel, and A. A. Demkov, Strain enhancement of the electro-optical response in BaTiO₃ films integrated on Si (001), *Phys. Rev. B* **98**, 075136 (2018).
- [12] F. Eltes, C. Mai, D. Caimi, M. Kroh, Y. Popoff, G. Winzer, D. Petousi, S. Lischke, J. E. Ortmann, L. Czornomaz *et al.*, A BaTiO₃-based electro-optic Pockels modulator monolithically integrated on an advanced silicon photonics platform, *J. Light. Technol.* **37**, 1456 (2019).
- [13] S. Abel, F. Eltes, J. E. Ortmann, A. Messner, P. Castera, T. Wagner, D. Urbonas, A. Rosa, A. M. Gutierrez, D. Tulli *et al.*, Large Pockels effect in micro- and nanostructured barium titanate integrated on silicon, *Nat. Mater.* **18**, 42 (2019).
- [14] M. Reynaud, Z. Dong, H. Park, W. Li, A. B. Posadas, J. H. Warner, D. Wasserman, and A. A. Demkov, Microstructural analysis and electro-optic properties of thick epitaxial BaTiO₃ films integrated on silicon (001), *Phys. Rev. Mater.* **6**, 095201 (2022).
- [15] A. B. Posadas, V. E. Stenger, J. D. DeFouw, J. H. Warner, and A. A. Demkov, RF-sputtered Z-cut electro-optic barium titanate modulator on silicon photonic platform, *J. Appl. Phys.* **134**, 073101 (2023).
- [16] M. Reynaud, H. Huyan, C. Du, W. Li, A. B. Posadas, X. Pan, and A. A. Demkov, Si-integrated BaTiO₃ for electro-optic

- applications: Crystalline and polarization orientation control, *ACS Appl. Electron. Mater.* **5**, 4605 (2023).
- [17] M. Reynaud, P. Y. Chen, W. Li, T. Paoletta, S. Kwon, D. H. Lee, I. Beskin, A. B. Posadas, M. J. Kim, C. M. Landis *et al.*, Microstructural analysis and electro-optic properties of thick epitaxial BaTiO₃ films integrated on silicon (001), *Phys. Rev. Mater.* **5**, 035201 (2021).
- [18] A. Rao and S. Fathpour, Heterogeneous thin-film lithium niobate integrated photonics for electrooptics and nonlinear optics, *IEEE J. Sel. Top. Quant. Electron* **24**, 1 (2018).
- [19] E. L. Wooten, K. M. Kissa, A. Yi-Yan, E. J. Murphy, D. A. Lafaw, P. F. Hallemeier, D. Maack, D. V. Attanasio, D. J. Fritz, G. J. McBrien *et al.*, Review of lithium niobate modulators for fiber-optic communications systems, *IEEE J. Sel. Top. Quant. Electron* **6**, 69 (2000).
- [20] D. Janner, D. Tulli, M. García-Granda, M. Belmonte, and V. Pruneri, Micro-structured integrated electro-optic LiNbO₃ modulators, *Laser Photonics Rev.* **3**, 301 (2009).
- [21] R. S. Weis and T. K. Gaylord, Lithium niobate: Summary of physical properties and crystal structure, *Appl. Phys. A* **37**, 191 (1985).
- [22] M. Veithen, X. Gonze, and P. Ghosez, Nonlinear optical susceptibilities, Raman efficiencies, and electro-optic tensors from first-principles density functional perturbation theory, *Phys. Rev. B* **71**, 125107 (2005).
- [23] A. K. Hamze and A. A. Demkov, First-principles study of the linear electro-optical response in strained SrTiO₃, *Phys. Rev. Mater.* **2**, 115202 (2018).
- [24] A. El Boutaybi, P. Karamanis, T. Maroutian, S. Matzen, L. Vivien, P. Lecoeur, and M. Rérat, Electro-optic properties of ZrO₂, HfO₂, and LiNbO₃ ferroelectric phases: A comparative density functional study, *Phys. Rev. B* **107**, 045140 (2023).
- [25] C. Paillard, S. Prokhorenko, and L. Bellaïche, Strain engineering of electro-optic constants in ferroelectric materials, *npj Comput. Mater.* **5**, 6 (2019).
- [26] I. Kim, T. Paoletta, and A. A. Demkov, Nature of electro-optic response in tetragonal BaTiO₃, *Phys. Rev. B* **108**, 115201 (2023).
- [27] I. P. Kaminow and E. H. Turner, Electrooptic light modulators, *Appl. Opt.* **5**, 1612 (1966).
- [28] S. H. Wemple and M. DiDomenico Jr, Electrooptical and nonlinear optical properties of crystals, in *Applied Solid State Science*, edited by R. Wolfe (Elsevier, New York, 1972), Vol. 3, pp. 263–383.
- [29] M. Veithen, X. Gonze, and P. Ghosez, First-principles study of the electro-optic effect in ferroelectric oxides, *Phys. Rev. Lett.* **93**, 187401 (2004).
- [30] L. R. Dalton, P. Günter, and M. Jazbinsek, *Organic Electro-Optics and Photonics: Molecules, Polymers and Crystals* (Cambridge University Press, Cambridge, 2015).
- [31] I. P. Kaminow and W. D. Johnston Jr, Quantitative determination of sources of the electro-optic effect in LiNbO₃ and LiTaO₃, *Phys. Rev.* **160**, 519 (1967).
- [32] F. Detraux and X. Gonze, Photoelasticity of α -quartz from first principles, *Phys. Rev. B* **63**, 115118 (2001).
- [33] L. Chen, Y. Yang, Z. Gui, D. Sando, M. Bibes, X. K. Meng, and L. Bellaïche, Large elasto-optic effect in epitaxial PbTiO₃ Films, *Phys. Rev. Lett.* **115**, 267602 (2015).
- [34] A. H. Romero, D. C. Allan, B. Amadon, G. Antonius, T. Applencourt, L. Baguet, J. Bieder, F. Bottin, J. Bouchet, E. Bousquet *et al.*, ABINIT: Overview and focus on selected capabilities, *J. Chem. Phys.* **152**, 124102 (2020).
- [35] X. Gonze, B. Amadon, G. Antonius, F. Arnardi, L. Baguet, J.-M. Beuken, J. Bieder, F. Bottin, J. Bouchet, E. Bousquet *et al.*, The ABINIT project: Impact, environment and recent developments, *Comput. Phys. Commun.* **248**, 107042 (2020).
- [36] X. Gonze, G.-M. Rignanese, M. Verstraete, J.-M. Beuken, Y. Pouillon, R. Caracas, F. Jollet, M. Torrent, G. Zerah, M. Mikami *et al.*, A brief introduction to the ABINIT software package, *Z. Kristallogr.* **220**, 558 (2005).
- [37] X. Gonze, J.-M. Beuken, R. Caracas, F. Detraux, M. Fuchs, G.-M. Rignanese, L. Sindic, M. Verstraete, G. Zerah, F. Jollet *et al.*, First-principles computation of material properties: The ABINIT software project, *Comput. Mater. Sci.* **25**, 478 (2002).
- [38] D. R. Hamann, X. Wu, K. M. Rabe, and D. Vanderbilt, Metric tensor formulation of strain in density-functional perturbation theory, *Phys. Rev. B* **71**, 035117 (2005).
- [39] J. P. Perdew, A. Ruzsinszky, G. I. Csonka, O. A. Vydrov, G. E. Scuseria, L. A. Constantin, X. Zhou, and K. Burke, Restoring the density-gradient expansion for exchange in solids and surfaces, *Phys. Rev. Lett.* **100**, 136406 (2008).
- [40] M. J. van Setten, M. Giantomassi, E. Bousquet, M. J. Verstraete, D. R. Hamann, X. Gonze, and G.-M. Rignanese, The PseudoDojo: Training and grading a 85 element optimized norm-conserving pseudopotential table, *Comput. Phys. Commun.* **226**, 39 (2018).
- [41] H. J. Monkhorst and J. D. Pack, Special points for Brillouin-zone integrations, *Phys. Rev. B* **13**, 5188 (1976).
- [42] G. Kresse and D. Joubert, From ultrasoft pseudopotentials to the projector augmented-wave method, *Phys. Rev. B* **59**, 1758 (1999).
- [43] G. Kresse and J. Hafner, *Ab initio* molecular dynamics for liquid metals, *Phys. Rev. B* **47**, 558 (1993).
- [44] G. Kresse and J. Furthmüller, Efficiency of *ab-initio* total energy calculations for metals and semiconductors using a plane-wave basis set, *Comput. Mater. Sci.* **6**, 15 (1996).
- [45] G. Kresse and J. Furthmüller, Efficient iterative schemes for *ab initio* total-energy calculations using a plane-wave basis Set, *Phys. Rev. B* **54**, 11169 (1996).
- [46] G. Kresse and J. Hafner, Norm-conserving and ultrasoft pseudopotentials for first-row and transition elements, *J. Phys.: Condens. Matter* **6**, 8245 (1994).
- [47] P. E. Blöchl, Projector augmented-wave method, *Phys. Rev. B* **50**, 17953 (1994).
- [48] A. Togo and I. Tanaka, First principles phonon calculations in materials science, *Scr. Mater.* **108**, 1 (2015).
- [49] M. R. Chowdhury, G. E. Peckham, and D. H. Saunderson, A neutron inelastic scattering study of LiNbO₃, *J. Phys. C* **11**, 1671 (1978).
- [50] S. K. S. Kojima, Composition variation of optical phonon damping in lithium niobate crystals, *Jpn. J. Appl. Phys.* **32**, 4373 (1993).
- [51] R. Claus, J. Brandmüller, G. Borstel, E. Wiesendanger, and L. Steffan, Directional dispersion and assignment of optical phonons in LiNbO₃, *Z. Naturforsch.* **27**, 1187 (1972).
- [52] G. K. Horton and A. A. Maradudin, *Dynamical Properties of Solids: Disordered Solids, Optical Properties* (North-Holland Publishing Company, Amsterdam, 1980), Vol. 4.

- [53] A. S. Barker Jr. and R. Loudon, Dielectric properties and optical phonons in LiNbO_3 , *Phys. Rev.* **158**, 433 (1967).
- [54] M. Veithen and Ph. Ghosez, First-principles study of the dielectric and dynamical properties of lithium niobate, *Phys. Rev. B* **65**, 214302 (2002).
- [55] A. P. Giddy, M. T. Dove, G. S. Pawley, and V. Heine, The determination of rigid-unit modes as potential soft modes for displacive phase transitions in framework crystal structures, *Acta Cryst. A* **49**, 697 (1993).
- [56] R. E. Cohen and H. Krakauer, Lattice dynamics and origin of ferroelectricity in BaTiO_3 : Linearized-augmented-plane-wave total-energy calculations, *Phys. Rev. B* **42**, 6416 (1990).
- [57] I. Inbar and R. E. Cohen, Comparison of the electronic structures and energetics of ferroelectric LiNbO_3 and LiTaO_3 , *Phys. Rev. B* **53**, 1193 (1996).
- [58] K. Toyoura, M. Ohta, A. Nakamura, and K. Matsunaga, First-principles study on phase transition and ferroelectricity in lithium niobate and tantalate, *J. Appl. Phys.* **118**, 064103 (2015).
- [59] A. Räuber, *Current Topics in Materials Science*, edited by E. Kaldis (North-Holland, Amsterdam, 1978), Vol. 1, p. 481.
- [60] F. Abdi, M. Aillerie, P. Bourson, M. D. Fontana, and K. Polgar, Electro-optic properties in pure LiNbO_3 crystals from the congruent to the stoichiometric composition, *J. Appl. Phys.* **84**, 2251 (1998).